Combining nonlinear vibration absorbers and the Acoustic Black Hole for passive broadband flexural vibration mitigation

Haiqin Li, Cyril Touzé, Adrien Pelat, François Gautier

Combining Nonlinear Vibration Absorbers and the Acoustic Black Hole for Passive Broadband Flexural Vibration Mitigation

Haiqin Li[a,*], Cyril Touzé[a], Adrien Pelat[b], François Gautier[b]

[a]*IMSIA, ENSTA Paris-CNRS-EDF-CEA, Institut Polytechnique de Paris, 828 Boulevard des Maréchaux, 91762 Palaiseau Cedex, France*
[b]*Laboratoire d'Acoustique de l'Université du Mans, UMR CNRS 6613, Av.O.Messiaen, 72085, Le Mans Cedex 9, France*

Abstract

The Acoustic Black Hole (ABH) effect refers to a special vibration damping technique adapted to thin-walled structures such as beams or plates. It usually consists of a local decrease of the structure thickness profile, associated to a thin viscoelastic coating placed in the area of minimum thickness. It has been shown that such structural design acts as an efficient vibration damper in the high frequency range, but not at low frequencies. This paper investigates how different types of vibration absorbers, linear and nonlinear, added to the primary system can improve the low frequency performance of a beam ABH termination. In particular, the conjugated effects of the Acoustic Black Hole effect and a Tuned Mass Damper (TMD), a Nonlinear Energy Sink (NES), a bi-stable NES (BNES), and a vibro-impact ABH (VI-ABH) are investigated. Forced response to random excitation are computed in the time domain using a modal approach combined with an energy conserving numerical scheme. Frequency indicators are defined to characterize and compare the performance of all solutions. The simulation results clearly show that all the proposed methods are able to damp efficiently the flexural vibrations in a broadband manner. The optimal tuning of each proposed solution is then investigated through a thorough parametric study, showing how to optimize the efficiency of each solution. In particular, TMD and VI-ABH show a slight dependence on vibration amplitude, while the performance of NES and BNES have a peak of efficiency for moderate amplitudes.

Keywords: Vibration damping; Acoustic Black Hole; Energy transfer; Nonlinear energy sink; Vibro-impact.
PACS: 62.30.+d
PACS: 05.45.-a

*Corresponding author.
  Email addresses:* `haiqin.li@ensta-paris.fr` (Haiqin Li), `cyril.touze@ensta-paris.fr` (Cyril Touzé), `adrien.pelat@univ-lemans.fr` (Adrien Pelat), `francois.gautier@univ-lemans.fr` (François Gautier)

1. Introduction

The Acoustic Black Hole effect (ABH) is a technique for passively mitigating structural vibrations in beams and plates. It usually consists of a local decrease of the structure thickness profile, associated to a thin viscoelastic coating placed in the area of minimum thickness. It has been shown that such structural design acts as an efficient vibration damper in the high frequency range [1] because of a wave trap effect induced by the flexural waves properties in thin-walled structures with variable thickness. Because of its potentiality for improving the performances of mechanical structures, and especially in light-weight structures, the scientific literature on this strategy has grown rapidly in recent years. Numerous studies have been realized on experimental and numerical viewpoints, and have confirmed the effectiveness of an ABH for passive control of vibration in the high frequency range.A detailed review of the theory and applications is provided in [2].

ABH techniques have been developed to reduce structural vibrations and the resulting structure-borne noise, especially in light-weight structures. Thanks to the decreasing thickness, the vibration field is strongly trapped into the tapered edge, where the damping properties of the added layer ensures a fast energy decay, counterbalancing the effect of a final non-zero thickness. Theoretical and numerical works have been conducted to model the low reection coefficient for flexural waves in beam, resulting from this mechanism [3, 4], to address the improvement on modal damping ratio and modal overlap factor [5], to optimize the design of configurations and damping layers [6–8], and to to interpret the ABH effect using the critical coupling concept [9]. Experimental evidence of ABH effect using a variety of beam-like and plate-like structures are also numerous [6, 10–13]. Recent analytical advances for the exact solutions of ABHs in beam structures are shown in [14], and the numerical and experimental contributions that aims at optimizing the design of ABHs for vibration suppression have been discussed in [15–19] for various structures. In addition, applications of ABH to other areas, including elastic metastructures [20], energy harvesting [21], vibro-impact systems [22] and cochlear systems, have also been investigated.

However, there is also a known drawback regarding the ABH strategy: namely, it is generally inefficient in the low-frequency range [5, 23]. In some recent contributions, it has been rigorously demonstrated that a cut-on frequency exists, below which the ABH may lose its effectiveness [24, 25]. Although in the aforementioned linear ABH structures, the cut-on frequency could be somehow reduced through certain optimizations, it is unfortunately unavoidable in any implementation. To overcome this drawback, the idea of combining an ABH with another vibration damping device might be a desirable way for producing broadband vibration mitigation.

A first idea is to use a tuned mass damper (TMD) [26, 27], which consists in a linear device added to the beam and tuned to one resonant mode. Based on the classical results presented in [26], it is known that the main parameter optimisation criteria follows analytical results in order to properly tune the stiffness and damping coefficients of the linear absorber. Effectiveness of a TMD in the case of linear single and multi degrees of systems has been proven to be a very reliable passive mitigation device in a large number of contexts [28]. Thus, once a TMD is attached to an ABH beam and tuned to one of its resonant mode in

2

the low frequency range, where the ABH effect is ineffective, a reduction on the resonance peaks could hence be awaited [29], and the average performance of the ABH in the low frequency could be improved.

The known major drawback of a TMD is that it is only effective in the neighborhood of a single frequency. To overcome this limitation and realize a more broadband vibration suppression, using a purely nonlinear vibration absorber such as an NES has become nowadays another classical method in order to obtain targeted energy transfer [30]. Unlike the TMD, the NES has no eigenfrequency and can tune to any frequency content displayed by the primary vibrating structure, thus achieving broadband vibration suppression [31, 32]. From this sense, an appropriately designed NES can outperform linear absorbers in many applications [33, 34]. However, since it relies on a nonlinear mechanism, the NES needs a minimal vibration energy in order to launch the targeted energy transfer, a drawback known as the energy barrier. Besides the classical cubic nonlinearity, there are also many other methods for realizing the nonlinear restoring force in the NES [35], such as piecewise nonlinearity, nonlinear damping [36, 37], and vibro-impact dynamics[38, 39]. Also, different experimental designs have been proposed, see *e.g.* [40–46].

Recent studies have considered the case of a negative linear stiffness to create a configuration of a Bistable Nonlinear Energy Sink (BNES), for which in particular has been shown that the minimal energy required to activate the energy transfer is reduced [47–49]. In this paper we thus want to use an NES or BNES to control more modes of the ABH below its cut-on frequency, and compare its performance to a TMD.

The third idea is to rely on a Vibro-Impact ABH (VI-ABH), recently introduced in [22], in order to enhance the low-frequency efficiency. Adding contact points on which the structure will impact during its vibration, the VI-ABH encompasses a non-smooth nonlinear effect creating fast transfers of energy to the high-frequency range where it is most efficiently damped. Note that such a strong nonlinearity is found to be much more efficient than geometrical nonlinearity, which has also been employed with the same idea to improve ABH in the low frequency range [50]. Vibro-Impact technique, although being different in nature from the addition of a vibration absorber, is contrasted to the other proposed approaches, in order to offer a comparative view of the improvements one can awaited.

This paper is organized as follows. Section 2 is devoted to the modeling of the considered systems, with a special emphasis on ABH beam and the implementation of added vibration absorber in the dynamics. The numerical results are then presented and compared in Section 3, where a thorough parametric study addresses the problem of optimizing the tuning of each vibration absorber in order to enhance the low-frequency efficacy. Section 4 concludes the article.

2. Modeling

The structures considered in this study are composed of a main ABH beam together with added vibration absorbers. Also, the case of a VI-ABH is contrasted in order to give more insight to the results with cross-comparisons between different solutions. Fig. 1 depicts the

3

cases under study, where Fig. 1(a) refers to an ABH beam with a vibration absorber (be it linear or nonlinear). The second configuration under study, the VI-ABH, is illustrated in Fig. 1(b). In this section, the focus is first put to the system shown in Fig. 1(a), while the VI-ABH is considered in section 2.3.

2.1. ABH with linear and nonlinear dampers

Considering at first the configuration in Fig. 1(a), and study the flexural vibrations of the ABH beam termination coupled to a vibration absorber. The ABH beam is of length L and width b, and its thickness h_b is uniform for $x \in [0, x_{abh}]$, x being the axial beam coordinate and follows a power-law profile for $x \in [x_{abh}, L]$

$$h_b(x) = \begin{cases} h_0, & \text{for } x \in [0, x_{abh}] \\ h_0 \left(\dfrac{x - x_{end}}{x_{abh} - x_{end}} \right)^2, & \text{for } x \in [x_{abh}, L]. \end{cases} \tag{1}$$

For such a tapered beam, the cross-section area $A(x)$ and the inertia moment $I(x)$ are also spatial dependent, and reads $A(x) = bh_b(x)$ and $I(x) = bh_b(x)^3/12$, respectively.
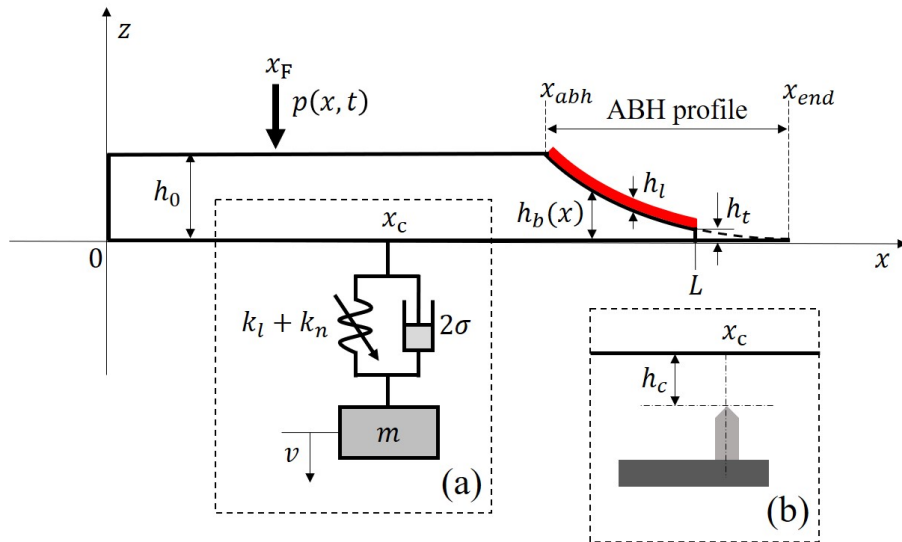

Fig. 1. Sketch of an ABH beam coupled to a vibration absorber or to a contact point, (a): configuration of a vibration absorber located at x_c, (b): configuration of a VI-ABH with a contact point located at x_c and characterized by a gap h_c. L is the total length of the beam, h_0, $h_b(x)$ and h_t are the thicknesses of the beam respectively in its uniform area, in the ABH profile, and at the ABH's tip, while h_l is the thickness of the ABH absorbing coating layer.

The vibration absorber is attached to the beam at the coupling point $x = x_c$. The absorber is characterized by its mass m (assumed to be small as compared to the beam mass), its damping coefficient 2σ, linear stiffness k_l, and nonlinear stiffness k_n.

4

Let $u(x,t)$ denote the transverse displacement of the beam, and $v(t)$ represent the motion of the coupled oscillator. In terms of an Euler-Bernoulli beam, the governing equations are written as [51, 52]

$$\rho(x)A(x)\frac{\partial^2 u}{\partial t^2} + \frac{\partial^2}{\partial x^2}\left(D^*(x)\frac{\partial^2 u}{\partial x^2}\right) = p\delta(x - x_F) - f\delta(x - x_c), \tag{2a}$$

$$m\ddot{v} = f, \tag{2b}$$

$$f = k_l w + k_n w^3 + 2\sigma\dot{w}, \tag{2c}$$

$$w = u(x_c, \ t) - v, \tag{2d}$$

where $D^*(x)$ is the complex bending stiffness, and $p = p(x,t)$ is the external excitation induced at $x = x_F$. The restoring force of the oscillator, $f = f(x,t)$, is written as a function of the relative motion $w = u(x_c, \ t) - v$ and characterized by three parameters: the linear stiffness k_l, the cubic nonlinear stiffness k_n, and a viscous damping term σ. Thus, by setting different values for k_l and k_n, different types linear or nonlinear vibration dampers can be obtained. The linear case for which $k_n = 0$ and $k_l > 0$ corresponds to a Tunable Mass Dampler (TMD) [26, 29]; while $k_l = 0, k_n > 0$ creates a classical NES with cubic nonlinearity [53, 54]. Finally, $k_l < 0, k_n > 0$ refers to the case of a BNES [49, 55]. For each system, the mass ratio $\epsilon = m/\int_0^L \rho(x)A(x)\,dx$ is defined as the ratio between the mass of the oscillator m and the total mass of the ABH beam.

In the usual implementation of an ABH beam termination as shown in Fig. 1, a viscoelastic layer is added at the tip in order to locally enhance the losses. Consequently the damping property of the full ABH stems from two parts: the structural damping in the tapered metallic beam and the local damping induced by the thin viscoelastic layer along the wedge termination. Both effects are here considered by using the Ross-Kerwin-Ungar model [50, 56], in which a complex bending stiffness $D^*(x)$ is introduced. The complete expression of $D^*(x)$ is detailed in Appendix A. Note that this approach assumes a linear viscoelastic behaviour but may encounter limitations in case of nonlinear viscoelasticity, see e.g. [57] and references therein. However comparisons with measurements shows that the linear assumption is well met for the structures under study. Besides, due to the added mass of the damping layer, an equivalent modification of the thickness $h(x) = h_b(x) + h_l$ and of the material density $\rho(x) = (\rho_b h_b + \rho_l h_l)/h$ are also implemented in the ABH area, where ρ_b and ρ_l are the densities of the ABH beam and the layer, respectively.

Finally, for the boundary conditions, the beam is considered to be clamped at $x = 0$ and free at $x = L$, so that:

$$\forall\, t, \ \ u(0,t) = 0, \ \ \left.\frac{\partial u}{\partial x}\right|_{x=0,t} = 0, \ \ \left.\frac{\partial^2 u}{\partial x^2}\right|_{x=L,t} = 0, \ \ \left.\frac{\partial^3 u}{\partial x^3}\right|_{x=L,t} = 0. \tag{3}$$

2.2. Modal approach and time integration

A modal approach is used to describe the forced response of the ABH beam coupled to the vibration absorber. The numerical implementation is similar to the one described in [22]

in the case of a VI-ABH configuration, and the interested reader is referred to this paper for more detailed explanations. For the sake of conciseness, the key points of the modelling are recalled here and the description is focused mainly on the coupling between the beam and the additional degree of freedom describing the absorber. Applying the standard modal expansion, the flexural displacement $u(x,t)$ can be rewritten as

$$u(x,t) = \sum_{k=1}^{N_m} \phi_k(x) q_k(t), \tag{4}$$

where $q_k(t)$ is the modal coordinate associated to mode $\phi_k(x)$, N_m is the total number of modes selected in the expansion. The mode functions are normalized with respect to mass such that, $\forall\, 1 \leq k, p \leq N_m$, $\int_0^L \rho(x) A(x) \phi_k(x) \phi_p(x) \mathrm{d}x = \delta_{kp}$, with δ_{kp} the Kronecker delta function.

Applying the modal expansion Eq. (4) into the equations of motion Eqs. (2), and projecting the dynamics on each eigenmode, one obtains:

$$\ddot{q}_k + 2\xi_k \omega_k \dot{q}_k + \omega_k^2 q_k = p\phi_k(x_F) - f\phi_k(x_c), \tag{5a}$$

$$m\ddot{v} = f, \tag{5b}$$

$$f = k_l w + k_n w^3 + 2\sigma \dot{w}, \tag{5c}$$

$$w = \sum_{k=1}^{N_m} q_k \phi_k(x_c) - v. \tag{5d}$$

where ω_k and ξ_k are respectively the circular eigenfrequency and the modal damping ratio. Eqs. (5) show how the original problem described by a partial differential equation is replaced by a set of oscillator equations depending on time only.

Before solving Eqs. (5), an eigenvalue problem should be calculated to determine $\phi_k(x)$, ω_k, and ξ_k for each mode of the ABH beam, see the details given in Appendix A. Once the eigenvalue problem solved, the last step of the numerical model resides in the time integration of Eqs. (5), which is realized following the numerical scheme proposed in [58]. The main advantage of the method is to combine an exact scheme for the linear (modal) part and an energy-conserving expression for the penalized nonlinear coupling force. The scheme can be directly applied to Eqs. (5), with a special attention paid to the extra degree of freedom of the attached vibration absorber, the details are in Appendix B.

2.3. VI-ABH

In order to offer an exhaustive comparative view on different techniques to enhance the low-frequency efficiency of the ABH, the results obtained by using added vibration absorbers, will be contrasted to the gains one can obtain with a vibro-impact ABH. This device, introduced in [22], consists of using the non-smooth nonlinearity generated at the contact point between the beam and a rigid barrier, in order to rapidly transfer energy to the high-frequency range. Following the general configuration depicted in Fig. 1(b), the

modeling of the VI-ABH has already been established in [22]. The interested reader is thus referred to [22] for a detailed presentation. For the sake of completeness, the key equations are briefly recalled in Appendix C.

For the numerical parameters used in this study, we rely on the convergence study that has already been realized in [22] for a VI-ABH case, which is also the system showing the most pronounced nonlinear effects and can be thus selected in order to find the most stringent conditions for numerical convergence. It was demonstrated that for a VI-ABH, with modes number $N_m = 50$ and sampling frequency $F_s = 640\text{kHz}$, and for contact parameters $\alpha = 1.5$ and $k_c = 10^{11}\text{Nm}^{-1.5}$, the dynamics of the system converges and the results are accurate enough. On the other hand, for the systems with nonlinear dampers, a choice with less modes $N_m = 20$ and smaller sampling frequency $F_s = 16\text{kHz}$ is sufficient for our studies.

3. Numerical Results

3.1. Parameters of the ABH beam and linear performance

A typical ABH beam, made in aluminium, and whose design is similar to the one of experimental beam demonstrators presented in [5], is selected. The parameters are listed in Table 1. Note that in the first line, A uniform beam of constant thickness is also defined, and will be used as a reference in order to highlight the ABH effect.

Beam parameters					
L(m)	$h_0(\text{mm})$	$b(\text{mm})$	$E_b(\text{pa})$	$\rho_b(\text{kg} \cdot \text{m}^3)$	$\eta_b(\%)$
0.8	4	20	70G	2700	0.2
ABH termination parameters					
$x_{abh}(\text{m})$	$x_{end}(\text{m})$	$h_t(\mu\text{m})$			
0.71	0.80685	20			
Visco-elastic layer at $[x_{abh}, L]$					
$h_l(\mu\text{m})$	$E_l(\text{Pa})$	$\rho_l(\text{kg} \cdot \text{m}^3)$	$\eta_l(\%)$		
400	10M	1000	160		

Tab. 1: Geometrical and material parameters for the studied ABH beam.

The input mobility defined as the ratio between the velocity and the input force spectra at x_F, is shown in Fig. 2 for both the reference (naked) beam and the ABH beam. The effect of the ABH is particularly significant in the high-frequency range. Following [24], the cut-on frequency for this typical ABH design can be calculated as $f_c = 374$ Hz, which gives a correct order of magnitude as compared to the observation of the mobility shown in Fig. 2. Indeed, from f_c the peaks amplitudes start to decrease strongly but the most pronounced effect starts after the sixth eigenfrequency, above 500 Hz, leading to excellent added damping properties with 25dB attenuation of the resonance peaks. Thus, the next Sections aim at enhancing the low-frequency performance of the ABH effect by adding a linear or a nonlinear vibration absorber. More particularly, our goal will be to improve the damping properties in the frequency range $[0, 500]$ Hz.
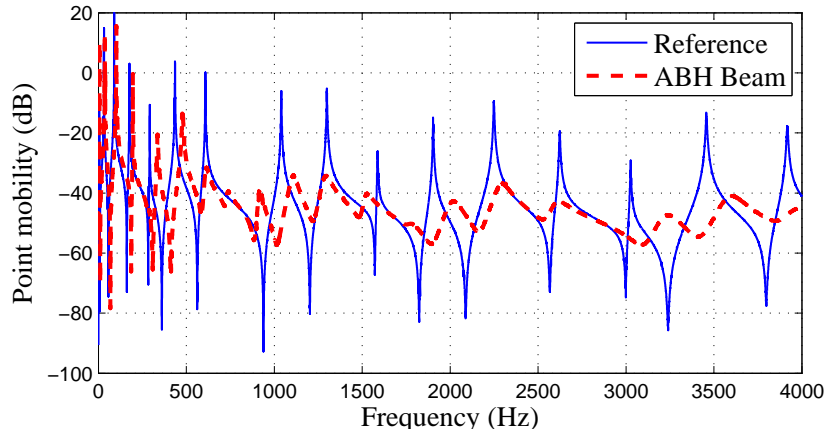
Fig. 2. Driving-Point mobility of the reference uniform beam (blue line), compared to that of an ABH beam (red line). Beam parameters are given in Table 1. A band-limited white noise excitation on $[0, 5000]$ Hz, with amplitude 1 N is appplied at $x_F = 24$ cm, which is point where the velocity is computed. Simulations parameters are: $F_s = 265$ kHz and N_m=50.

3.2. Effect of vibration absorbers on the low frequency modes

The numerical investigations are realized with a band-limited white noise excitation in the low frequency range $[0, 500]$ Hz, in order to test the improvement that can be awaited by adding vibration absorber to the ABH beam. Five different cases are first exhibited. The ABH beam is now selected as the reference case, and its damping efficiency in the low-frequency range is contrasted with 1/ ABH with an attached TMD, 2/ ABH with an attached NES with pure cubic stiffness, 3/ ABH with a BNES of cubic stiffness and negative linear stiffness, and with 4/ a VI-ABH. Fig. 3 shows the obtained results, where the velocity spectrums at the exciting point for each case are compared. It should be emphasized that for all the cases shown in Fig. 3, their parameters are arbitrarily selected without any optimization rule. The best tuning for the parameter of each absorber will be studied in the next section. Here, the purpose is to illustrate the effects associated to a not optimized configuration.

Fig. 3(a) shows the velocity spectrum for the five cases on the frequency range $[0, 800]$ Hz, and three zooms around the first peaks are shown in Fig. 3(b-d) in order to have a better of view of the details of the spectra. In particular, the zooms show that peaks corresponding to the eigenfrequencies of modes 2 and 3, can be efficiently reduced, whatever the tested solution. On the other hand, the first peak is less reduced, and only the VI-ABH is able to replace this sharp peak by a fuzzy spectrum in this range. Fig. 3(e) shows the ratio of velocity spectrum divided by the excitation spectrum, in order to highlight the low-frequency differences. This underlines in particular the linear behaviour of the TMD and the nonlinear behaviour of all other solutions.

It is clear that each method can bring effective reductions on the resonance peaks at low frequency of the ABH beam. In this typical comparison, the reductions for the first 4 modes
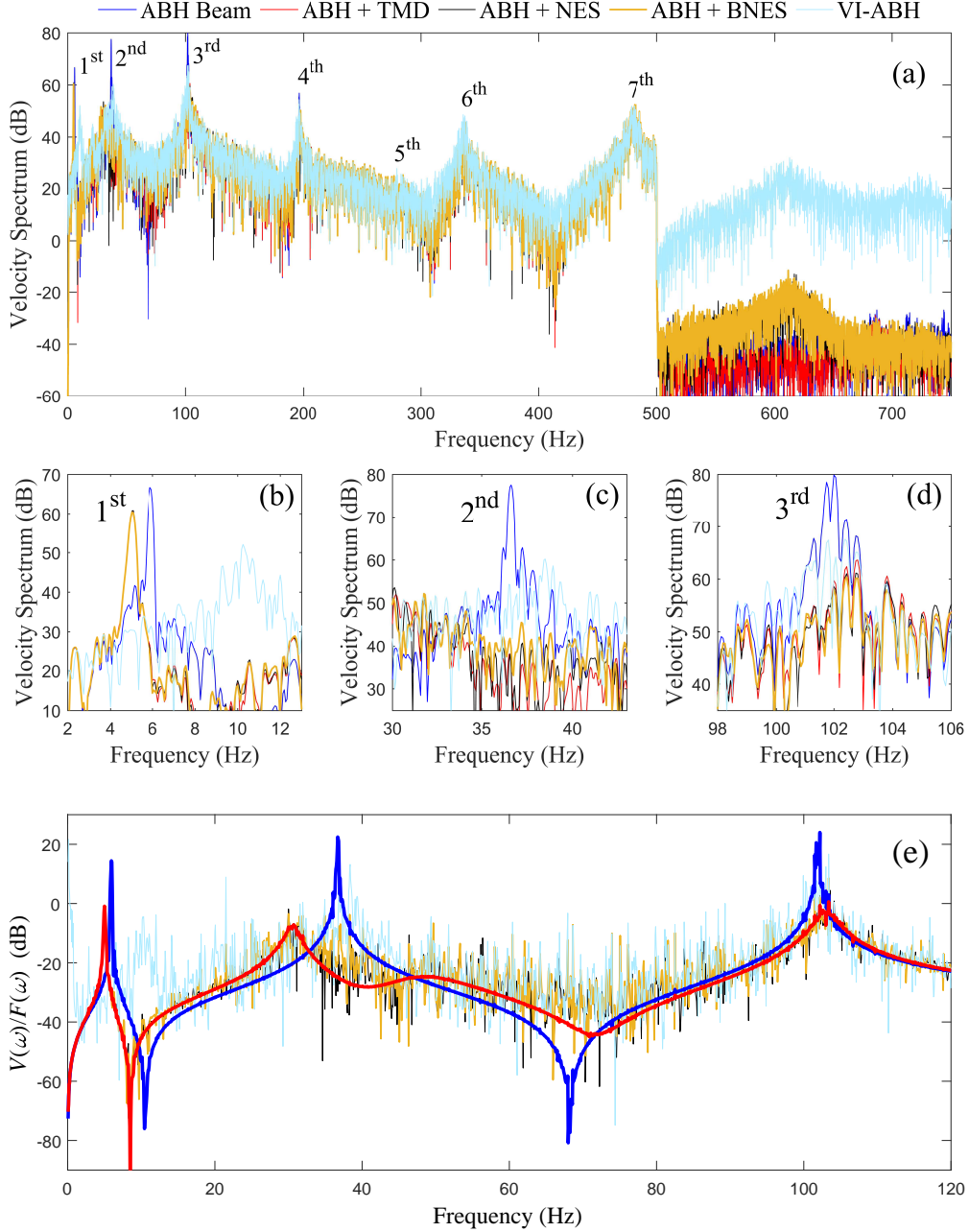
8

Fig. 3. Reduction of resonance peaks of the ABH beam by using TMD, NES, BNES and VI-ABH,(a): velocity spectrum over $[0, 500]$ Hz, (b-d): zooms of velocity spectrum at mode 1-3, (e): point mobility. The parameters are $k_l = 800$ N/m and $\sigma = 0.5$N $\cdot$ s/m for TMD; $k_n = 3 \times 10^9$ N/m^3 and $\sigma = 0.5$N $\cdot$ s/m for NES; $k_l = -300$ N/m, $k_n = 3 \times 10^9$ N/m^3 and $\sigma = 0.5$N $\cdot$ s/m for BNES, and $k_c = 3 * 10^9$N/m$^\alpha$, $\alpha = 1.5$ for VI-ABH. For all the cases, $x_c = 0.72$ m, the beam is excited a white noise of $[0, 500]$ Hz, with amplitude $A = 5$ N and location $x_F = 0.24$ m, and the dynamics are simulated up to 10s.

are extremely significant, while for mode 5-7 it is less important. Inspecting the zooms, one can see that for mode 2, there are around 15-25dB reduction of the resonance, depending on the typical methods selected, and for mode 3 there are also around 10-20dB reduction by using different nonlinear absorbers. Thus, it is proved that by using a nonlinear absorber, the performance of the ABH beam at the low frequency range is highly improved. Moving to the spectrum above 500Hz, one can find that a VI-ABH leads to significant energy transfer to the high frequency part. On the other hand, the nonlinearity of the NES and the BNES also brings a transfer to the high frequency range, but with less intensity than the VI-ABH, resulting from the fact that the nonlinearity is smoother. Finally the TMD shows no such energy transfer, in line with its linear behaviour.

In order to assess the improvements of the above strategies from a more quantitative point of view, an indicator that compares the power spectrum in different frequency bands is then introduced as

$$I = 10\log_{10}\left(\frac{\int_{f_0}^{f_{end}} V_c^2 \, \mathrm{d}f}{\int_{f_0}^{f_{end}} V_{ref}^2 \, \mathrm{d}f}\right), \tag{6}$$

where V is the output velocity spectrum at the excitation point $x = x_F$, and the subscript ref or c stands respectively for the reference case (*i.e.* the ABH beam with no absorber) and a current tested case (*i.e.* the ABH with an absorber). This frequency indicator allows one to evaluate the gains on vibration reduction in the frequency interval $[f_0, f_{end}]$. More precisely, in order to compare the performance of linear and nonlinear vibration absorbers in the low frequency range, several indicators defined in different frequency bands are listed in Tab. 2. With these definitions, indicators I_{ω_1} to I_{ω_7} allows quantifying the reduction of resonance peaks near each of the low eigenfrequency ω_1 to ω_7, that are below the cut-on frequency of the ABH beam; while I_{ave} denotes the average perfomance at the low frequency band [0, 500] Hz of the ABH beam.

Indicators	I_{ω_1}	I_{ω_2}	I_{ω_3}	I_{ω_4}	I_{ω_5}	I_{ω_6}	I_{ω_7}	I_{ave}
$\omega_i/2\pi$ (Hz)	5.9	36.7	101.9	196.2	278.5	336.5	478.9	/
f_0 (Hz)	0	30	95	190	260	320	460	0
f_{end} (Hz)	15	45	110	205	300	360	500	500

Tab. 2: Indicators defined in different frequency bands

The indicators for the cases shown in Fig. 3 are then calculated and summarized in Fig. 4. Note that as the beam is subjected to a white noise excitation, a single simulation result may not give an accurate value for the indicators, due to the randomness of the chosen excitation signal. To obtain a converged result, a Monte Carlo method is applied, and the indicators for each case are obtained as the average values over 20 random selections. Specifically, the average values for each indicator I_{ω_1} to I_{ave}, together with the standard variations are depicted in Fig. 4. One can see that the variations brought by the randomness of the excitation may be significant. The worst case is for I_{ω_1} and I_{ω_2}, with a variation range on the result around ±6dB. On the other hand, the indicators are less prone to variations

due to randomness for the higher frequencies. Finally, for the average performance I_{ave}, the variation is around ± 1.5dB. These observations are clearly related to the length of the time simulations as compared to the eigenfrequency. This means that a single simulation is not sufficient to provide accurate values for each indicator. The convergence analysis of I_{ave} for the BNES case is shown as an example in the subfigure, where the average value of I_{ave} is shown as a function of the number of simulation samples for averaging. It is then concluded that, at least 5 times of simulation samples should be considered for calculating the value I_{ave}, and the values of I_{ave} can be converged to to a very small variation of 0.2dB. In this paper hereafter, for each case, we will make 10 times of simulations, and take the average value calculated in each case for the indicators.
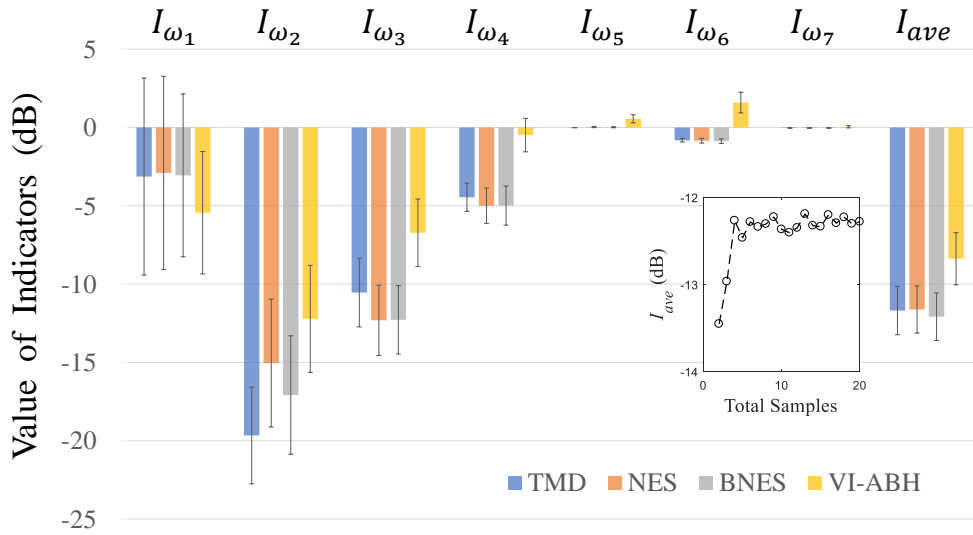

Fig. 4. Histograms of Indicators I_{ω_1} to I_{ave} calculated for the four cases in Fig. 3, statistics on the average value and standard variations, calculated from 20 randomly generated white noise excitations with amplitude 5N and frequency band $[0, 500]$Hz. The subfigure shows the convergence for the average value of I_{ave} as the number of sample size increases from 2 to 20

In the next sections, with the help of the indicators, the parametric effect for each strategy will be discussed with respect to different frequency ranges, in order to give some guidelines on the design of the nonlinear dampers.

3.3. Tuning the vibration absorbers: parametric study

In this section, the tuning methodology to optimize the performance of the different vibration absorbers, is investigated thanks to a thorough parametric study. The parameters to investigate are: the linear stiffness k_l, the cubic nonlinear stiffness k_n, the location x_c, the mass ratio ϵ and the damping coefficient σ. Note that in this section, the investigations are focused on the cases of the absorbers. The comparison with the VI-ABH is postponed to

section 3.4 where the effect of the vibration amplitudes will also be taken into account in order to test the efficiency of the nonlinear strategies with respect to amplitude.

3.3.1. Effect of stiffness

The effect of linear and nonlinear stiffness coefficients is first investigated since it plays an important role for the energy transfer between the ABH and the dampers. To that purpose, the other parameters are fixed as x_c=0.72m, σ=0.5Ns/m, and $\epsilon = 0.1$ for all the simulations, and the excitation is a white noise frequency bandwidth limited to $[0, 500]$Hz, with amplitude $A = 5$N and location $x_F = 0.24$m. The first case investigated is that of the TMD, for which the values of different indicators for varying linear stiffness k_l is depicted in Fig. 5.
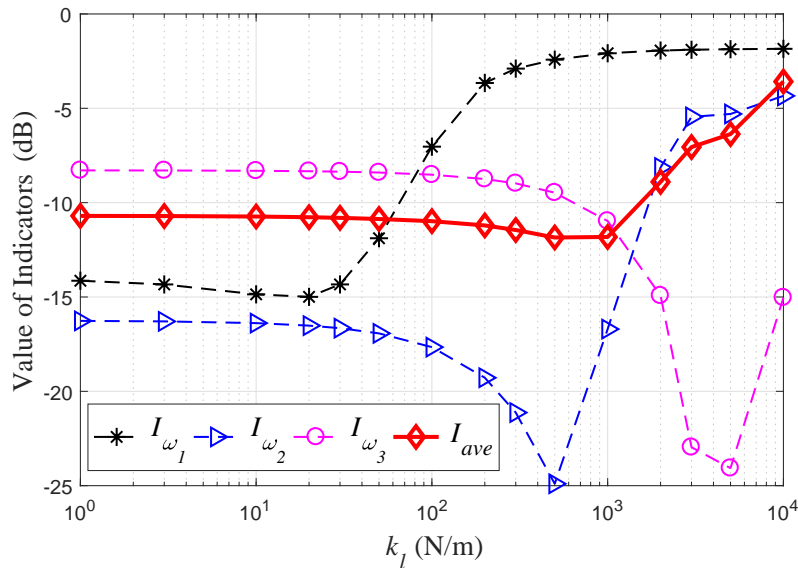

Fig. 5. Case of the ABH beam with an attached TMD. Variation of indicators I_{ω_1}, I_{ω_2}, I_{ω_3}, and I_{ave} as functions of the TMD linear stiffness k_l. Other parameters as x_c=0.72m, σ=0.5Ns/m, and $\epsilon = 0.1$.

It can be seen that as k_l increases, I_{ω_1}, I_{ω_2}, I_{ω_3}, and I_{ave} show a similar trend, with a different minimum value for each indicator. More specifically, I_{ω_1} meets its optimal value of $I_{\omega_1} = -15$dB for $k_l = 20$N/m, meaning a best reduction of the resonance peak at the first mode. For I_{ω_2} and I_{ω_3}, the optimal stiffness are $k_l = 500$N/m and $k_l = 5000$N/m, respectively. Since the linear stiffness of the TMD needs to be consistent with the eigenfrequency of the mode one wants to control, this behaviour is logical but prevent for finding out an optimal value for all the modes. Nevertheless, the combined effects reported by I_{ave} shows that a global minimum can be found for k_l around 1000N/m.

The optimal values found for controling each mode needs to be compared with the tuning rules prescribed for a TMD, where the known methods is to select the eigenfrequency of the TMD close to that of the mode under control, following the famous Den-Hartog rule based

on the equal peak method [26]. Using for example the formulas given in [28, 29, 59], optimal values for the stiffness k_l and the damping σ can be calculated as,

$$k_l = m \left(\frac{1 + \omega_i}{1 + m\phi_i^2(x_c)} \right)^2, \quad \sigma = m\omega_i \sqrt{\frac{3m\phi_i^2(x_c)}{8(1 + m\phi_i^2(x_c))^3}}. \tag{7}$$

with m the mass of the absorber, ω_i the ith eigenfrequency of the beam, and $\phi_i(x_c)$ the value of the ith mode function at location x_c. Thus, for mode 2, the optimal stiffness could be found at $k_l = 617\text{N/m}$, which is quite close to the value shown in Fig. 5.

We now turn to the case of an attached NES to the ABH beam. Fig. 6 shows the behaviours of the indicators as a function of the nonlinear stiffness k_n, where similar trends can be observed as compared to the TMD case. The optimal performance for the reduction of modes 1-3 could be respectively found as $k_n = 10^7\text{N/m}^3$ for I_{ω_1}=-15dB, $k_n = 10^9\text{N/m}^3$ for I_{ω_2}=-23dB, and $k_n = 3 \times 10^{10}\text{N/m}^3$ for I_{ω_3}=-20dB. The best average performance occurs when $k_n = 2 \times 10^9\text{N/m}^3$. Comparing to the prescriptions given in the literature, see *e.g.* [34, 49, 55], the general procedure derives from the analysis of the slow invariant manifold (SIM) of the system. More precisely, the system possesses a SIM that can be calculated analytically, showing a 'S' shape with two folding points, and the optimal design needs to adjust the parameters of NES so that the dynamical regime of the system are in the vicinity of the higher folding point of the SIM. In this case, the 1:1 resonance is highly excited, a special response regime referred to as Strongly Modulated Response (SMR) could exist, representing the most efficient dynamical mechanism for vibration suppression. In parallel to the Eq.(15) derived in [55], by reducing the dynamics discussed in our case to a given single mode i, this aforementioned SIM could hence be obtained analytically, together with a critical value of k_n for the folding point

$$k_n(\omega_i) = \frac{4m\omega_i^2}{9|w|^2} \left[2 + \sqrt{1 - 3\left(\frac{2\sigma}{m\omega_i} \right)^2} \right] \tag{8}$$

with $|w|$ the amplitude of the relative motion between the damper and ABH beam. Thus, for the optimal performance of I_{ω_i}, the optimal value of k_n should be adjusted close to the critical value given in Eq. (8).

Comparisons of the results shown in Fig. 6 with the value proposed in (8) shows a good matching. For example, Fig. 6 shows that the optimal performance for I_{ω_2} is obained for $k_n = 10^9\text{N/m}^3$. Using an amplitude of $|w|$ is around 1mm in line with the simulation, the analytical approximation for the value of $k_n(\omega_2)$is found to be $k_n(\omega_2) = 1.2 \times 10^9\text{N/m}^3$. For I_{ω_3}, our numerical result shows an optimal value of $k_n = 3 \times 10^{10}\text{N/m}^3$. Using a relative vibration amplitude $|w|$ of 0.6mm, again in line with the simulation where decreasing amplitudes are found for increasing frequencies, the analytical prediction gives $k_n(\omega_3) = 2.6 \times 10^{10}\text{N/m}^3$, showing again a very good agreement.

The third case under study is that of adding a BNES to the ABH beam. Fig. 7(a-c) gives the variation of indicators as function of the negative linear stiffness k_l, for three different
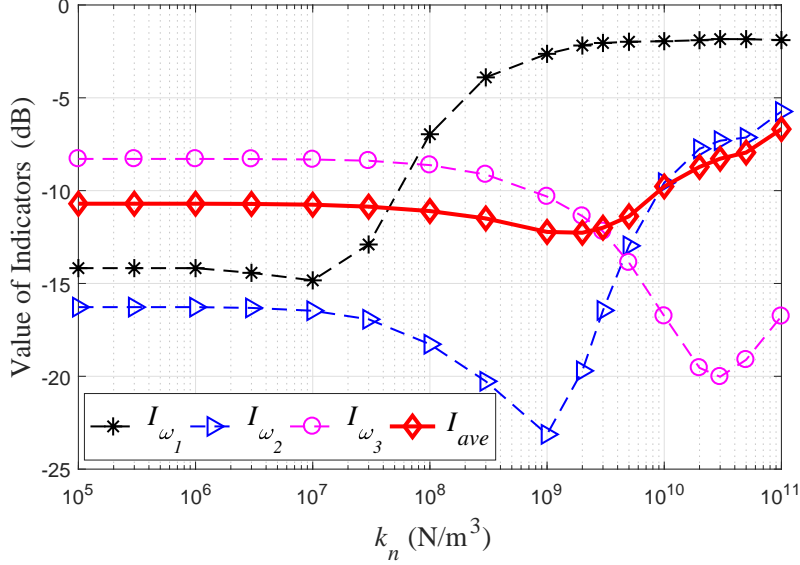
Fig. 6. Case of the ABH beam with an attached NES. Variation of indicators I_{ω_1}, I_{ω_2}, I_{ω_3}, and I_{ave} as functions of the nonlinear stiffness k_n. The other parameters for the NES are x_c=0.72m, σ=0.5Ns/m, and $\epsilon = 0.1$

values of the cubic stiffness: $k_n = 10^6 \mathrm{N/m^3}$, $k_n = 3 \times 10^7 \mathrm{N/m^3}$, and $k_n = 2 \times 10^9 \mathrm{N/m^3}$. One can observe that the behaviours of the indicators strongly depend on the value of the nonlinear stiffness k_n. While for small values of k_n the effect of varying k_l is important, the variations are far less noticeable for the third selected value of k_n. For $k_n = 10^6 \mathrm{N/m^3}$, the optimal performance can be easily observed as $k_l = -10 \mathrm{N/m}$ for I_{ω_1}, $k_l = -300 \mathrm{N/m}$ for I_{ω_2}, and $k_l = -2000 \mathrm{N/m}$ for I_{ω_3}, and the optimal average performance is obtained within $k_l \in [300, 500]$ N/m. These optimal values of the negative stiffness for each indicator remain almost the same when k_n increases up to $k_n = 3 \times 10^7 \mathrm{N/m^3}$.

These optimal values can be contrasted with the prescription given in [49], in which a simple framework for tuning a BNES in discrete system under impulse excitation is proposed. This study points out that, with respect to the high-amplitude cross-well oscillations, the negative stiffness k_l should be tuned targeting the vicinity of the natural frequency of the primary system, in the same fashion as for the classical linear TMD. Applying this rule to our case implies that the optimal value of $-k_l$ for I_{ω_1}, I_{ω_2} and I_{ω_3} should be tuned at the same order compared to the optimal values shown in Fig. 5 for each corresponding indicator, which of course shows a good agreement. In another research led in [55], the optimization of k_l is determined by using a Melnikov method, and found to be the local minimum of the function $\mathcal{M}(k_l)$:

$$\mathcal{M}(k_l) = \left(\frac{-k_l}{m\omega_i^2}\right)^{3/2} \cosh\left(\frac{\pi}{2}\sqrt{\frac{m\omega_i^2}{-k_l}}\right), \qquad (9)$$
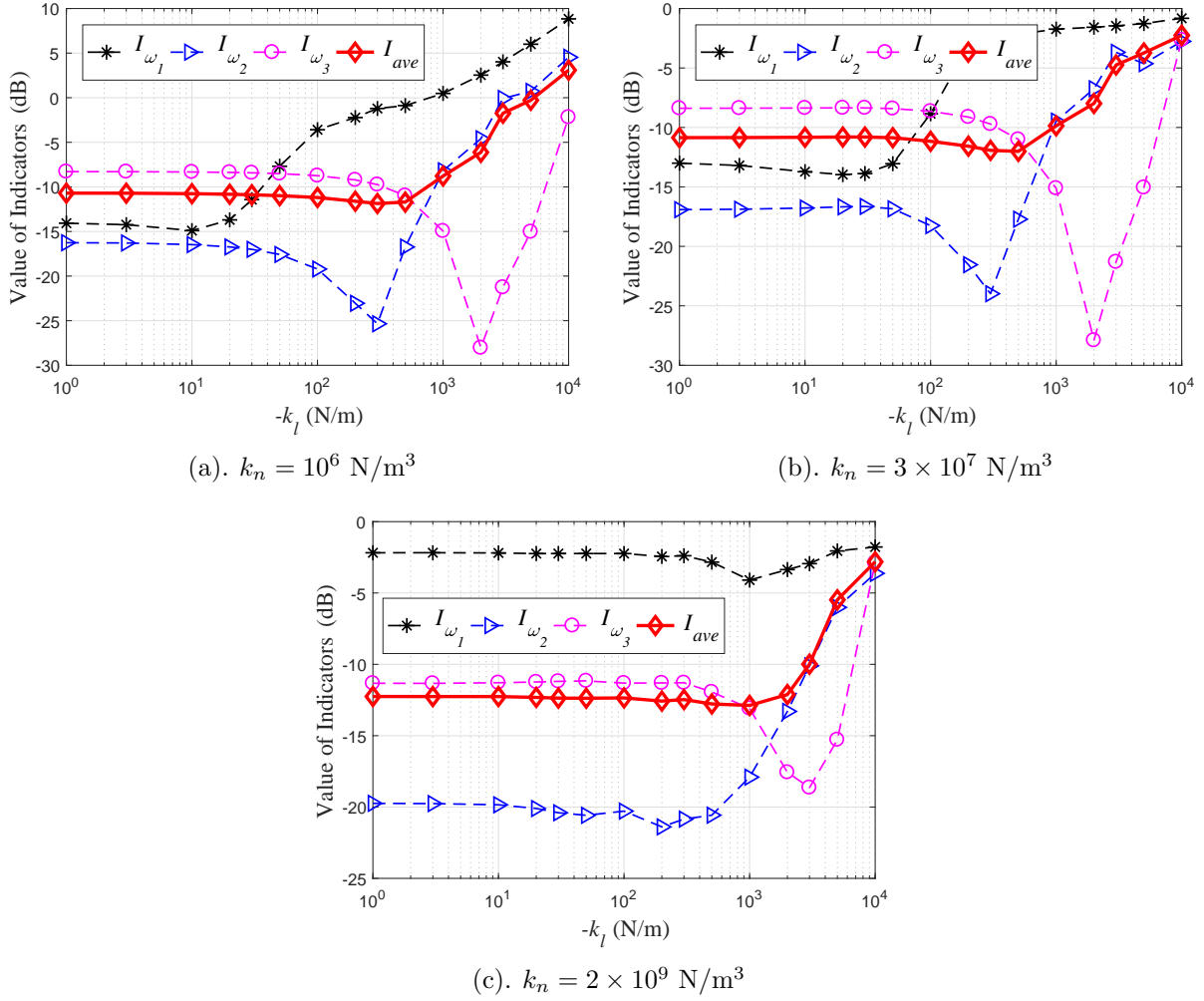
14

Fig. 7. Case of an ABH beam with an attached BNES. Variations of indicators I_{ω_1}, I_{ω_2}, I_{ω_3}, and I_{ave} as functions of the linear stiffness $-k_l$, for three different values of k_n: (a) $k_n = 10^6$ N/m^3 , (b) $k_n = 3 \times 10^7$ N/m^3, (c) $k_n = 2 \times 10^9$ N/m^3. Other parameters for the BNES are x_c=0.72m, σ=0.5Ns/m, and $\epsilon = 0.1$

for each eigenfrequency ω_i. Hence, the optimal values for each mode can be found as $k_l = -6.3$N/m for I_{ω_1}, $k_l = -245$N/m for I_{ω_2}, and $k_l = -1885$N/m for I_{ω_3}. These values are again consistent with our numerical findings reported in Fig. 7(a-b).

However, in Fig. 7(c) reports a quite different behaviour. In this case, the nonlinear stiffness $k_n = 2 \times 10^9$N/m^3 has been tuned to the optimal value found for the NES. The effect of k_l becomes less important, and increasing the values of k_l does not bring an evident improvement since the indicators remain stable at a wide range of k_l. This can be explained by the fact that in this case, the dynamical behaviour is dominated by the nonlinear stiffness. Consequently the effect of having a (now small) linear negative stiffness is negligible and the dynamics of the damping mechanism is dominated by that of a classical NES with targeted

energy transfer. To conclude this analysis, one can remark that in all the cases shown in Fig. 7(a-c), the performance is largely reduced when the negative linear stiffness becomes too large, testified by the sharpe increase of I_{ave} for $k_l < -1000$.

3.3.2. Effect of the location of the absorbers: a relationship to the mode shapes

Another interesting parameter is x_c, the location of the damper on the ABH beam. Considering first its effect on each single mode, Figs. 8(a-c) shows respectively how I_{ω_2}, I_{ω_3} and I_{ω_7} depends on x_c, for the three tested absorbers: TMD, NES and BNES. Interestingly, the remarkable effect on the value of the indicators is directly connected to the mode shape of the targeted mode, whatever the absorber is mounted on the ABH beam. More specifically, the value of the indicator I_{ω_i} is exactly proportional to the mode shape of the given mode, as depicted in Figs. 8(a-c) where the absolute (negative) value of each mode shape with a selected amplification factor has been reported as an eyeguide. Hence, in order to have the best performance for the reduction of a given mode, the linear or nonlinear dampers should be located at a local maximum of the given mode.

Even though a clear grasp of the underlying physical phenomenon is found for each mode, the combined effects on the average value I_{ave} depend on the relative position of eigenfrequencies, resulting in a pattern shown in Fig. 8(d). For all the dampers, the optimal position is located at the end of the beam. However, due to the ABH profile marked with a gray zone in Fig. 8, the thickness starts to severly decrease from $x = 0.71$m in the selected design. Consequently, for practical reasons, it does not appear as desirable to set a damper in this region of small thickness where the beam is weaker. Concentrating on the region of constant thickness, two optimal positions are clearly pointed out for the NES and BNES cases, respectively near $x_c = 0.24$m and $x_c = 0.44$m. One can also observe a different behaviour on I_{ave} between the TMD and the nonlinear dampers. While the two nonlinear vibration absorbers have two clear minimas at $x_c = 0.24$m and $x_c = 0.44$m, the TMD reaches a plateau in the range $x \in [0.2, 0.55]$m, and is not able to produce averaged improved performance below -4dB. This important conclusion that the performance of the nonlinear absorbers are more sensitive to the location as compared to the TMD has already been noted in previous study, see for example [60].

3.3.3. Effect of damping and mass ratio

The effect of the mass ratio on the performance is depicted in Fig. 9(a). One can easily conclude that the value of $\epsilon = 0.05$ gives a critical threshold: for ϵ below this value, increasing the mass ratio leads remarkable improvements on the performance of the absorbers, while for $\epsilon > 0.05$, no significant changes are evidenced by increasing the mass ratio. From a practical point of view, it is higly desirable to have the best reduction with the smallest possible added mass. Consequently the mass ratio of 0.05 is recommended as an appropriate choice.

All the three absorbers show similar interesting trend with respect to variations of the damping, as depicted in Fig. 9(b). When the internal damping of the absorber increases, the performance improves at first and then decreases in each case. This means neither too large nor to small damping is appropriate for effective vibration suppression. For too small values of damping, the absorber might be insufficient to damp out the energy, while
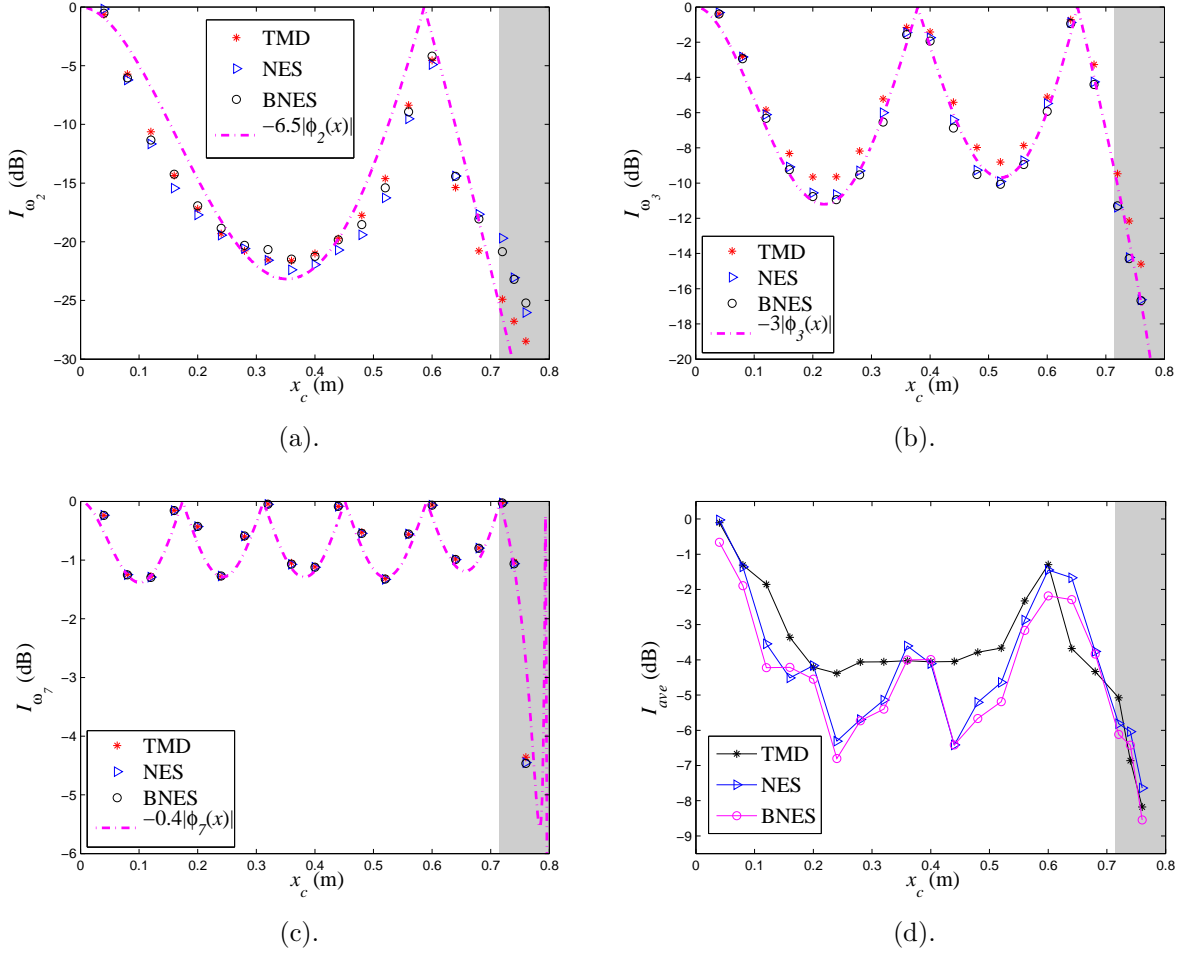
Fig. 8. Effect of position x_c on the value of Indicators, compared among the TMD with $k_l = 500\mathrm{N/m}$, NES with $k_n = 2 \times 10^9\mathrm{N/m}^3$, and BNES with $k_n = 2 \times 10^9\mathrm{N/m}^3$ and $k_l = -300\mathrm{N/m}$, (a-c): value of I_{ω_2} I_{ω_3}, and I_{ω_7}, (d): value of I_{ave}. The damping for each vibration damper is selected as $\sigma = 0.5\mathrm{N \cdot s/m}$ for (a-c) and $\sigma = 0.05\mathrm{N \cdot s/m}$ for (d). In each figure, the gray area refers to the ABH profile.

on the other hand a too large value reduces the relative motion between the beam and the absorber. As a result the appropriate selection of damping could be $\sigma = 3\ \mathrm{N \cdot s/m}$ for the best suppression. Moving on the difference among the TMD, NES and BNES, one can find that at low damping level, the difference among each case is important, NES and BNES can have a better behaviour than the TMD due to their strong nonlinearity. However these differences softens when the damping increases since overdamped motions renders the activation of the nonlinear phenomena more difficult.
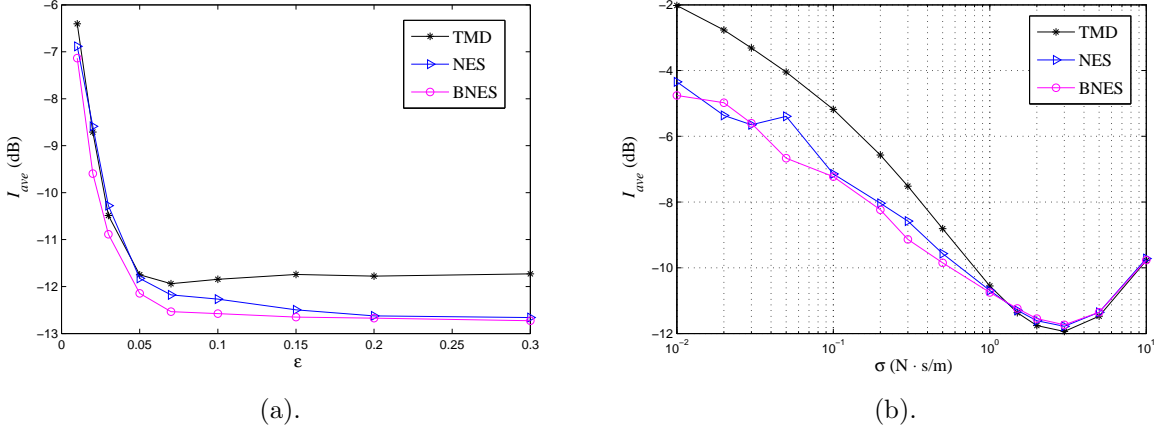
Fig. 9. Effect of mass ratio and damping on the value of indicator I_{ave}, compared among the TMD with $k_l = 500\text{N/m}$, NES with $k_n = 2 \times 10^9\text{N/m}^3$, and BNES with $k_n = 2 \times 10^9\text{N/m}^3$, $k_l = -300\text{N/m}$, (a): effect of mass ratio ϵ varies, with damping fixed at $\sigma = 0.5\text{N}\cdot\text{s/m}$, (b): effect of damping σ varies, while mass ratio fixed at $\epsilon=0.1$

3.4. Comparison of nonlinear absorbers and VI-ABH

This section is devoted to comparing the performance of added vibration absorber to the VI-ABH, which has been designed in order to offer a better vibration mitigation in the low-frequency range. The VI-ABH has been introduced and studied in [22]. It relies on a different nonlinear mechanism than that used in the nonlinear vibration absorber, even though some common points with recently studied vibro-impact NES can be traced [38, 39, 44]. However the VI-ABH does not consider and added oscillator representing a vibration absorber but only external contact points on which the beam will impact. At each impact, the strongly nonlinear behaviour transfers fastly energy to the high-frequency range where it is damped by the ABH properties. Since a special focus on the nonlinearity is also at hand with the comparison to VI-ABH, the effect of the vibration amplitudes on the efficacy of each solution, is also investigated.

3.4.1. Performance of a VI-ABH

The optimization of a VI-ABH has already been investigated in [22], with a special emphasis on finding out the best arrangement of numerous contact points on the beam, in order to achieve a strong improvement of the damping capacity of the ABH. Here, for the sake of comparison with adding a single vibration absorber, the effect of a single contact point is first investigated. Two parameters are to be tuned in that case: the contact stiffness k_c and the contact point position x_c. Variations of indicators as functions of these two parameters are shown in Fig. 10, respectively. As the contact stiffness increases, all the indicators decreases first and then remains stable. This behaviour is quite different from the ones found for the vibration dampers. As a result, the level of $k_c = 10^8\text{N/m}^{3/2}$ is critical; above this value, the contact is rigid enough and the values of the indicators tend to be stable.
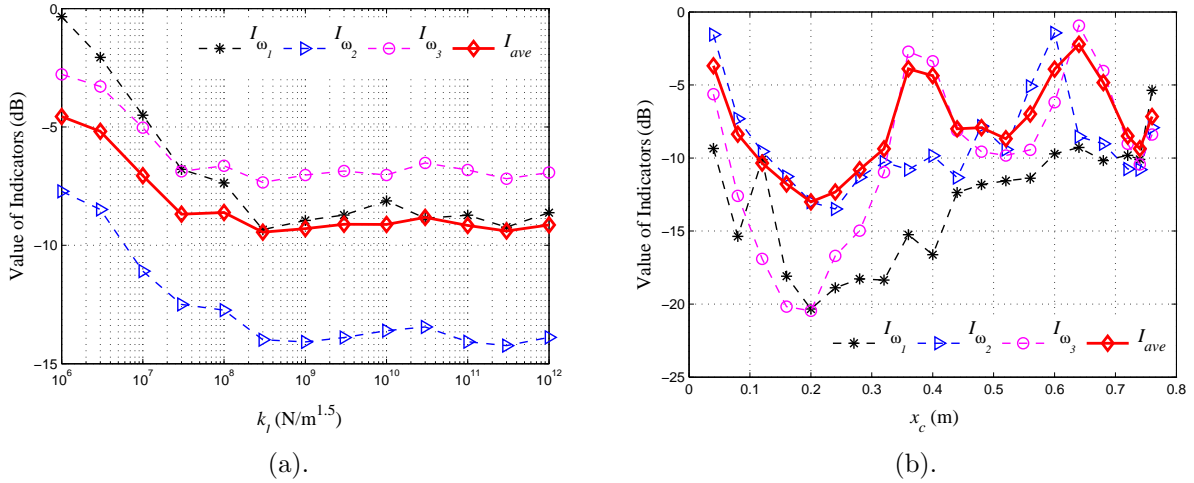
18

Fig. 10. Variation of indicators I_{ω_1}, I_{ω_2}, I_{ω_3}, and I_{ave} for the VI-ABH beam, as a fuction of: (a) the contact stiffness k_c (with $\alpha = 1.5$ and $x_c = 0.72$m), and (b) the location x_c (with $\alpha = 1.5$ and $k_c = 10^9$N/m$^{3/2}$).

The effect of x_c for the VI-ABH case is also quite different from the case of with linear and nonlinear dampers. First of all the value of the indicators are not directly proportional to the value of the mode shape function. Here, the position of the excitation point also have an impact, when the location of the contact point x_c is close to both the local maximum of the given mode and the exciting position x_F, the optimal reduction of the resonance peaks is obtained. For average performance, the optimal location of the contact point is around $x_c = 0.2$m.

3.4.2. Dependence on the vibration amplitude

The last parameter to be studied for offering an exhaustive comparisons of the behaviour of the nonlinear dampers, is the vibration amplitude. Indeed, for the cases of NES, BNES and VI-ABH, a nonlinear mechanism is at hand in order to produce the damping mechanism. It is also known from the literature on NES and BNES that an energy barrier exists for these vibration absorber: they are not active for too small vibration amplitude, and this barrier is advocated to be smaller in the case of a BNES.

The effect of the forcing amplitude on the values of I_{ω_2} and I_{ave} are shown in Fig. 11, for seven different cases. The case of the VI-ABH is reported with a red line and diamond markers, and one can observe that the performance of the VI-ABH shows a slight increase with the vibration amplitude. The three vibration absorbers (TMD in black, NES in blue and BNES in magenta) are then contrasted to this result, and for two different values of parameters. The solid lines refers to the case where the optimal parameters have been selected for each solution, while the dashed lines show how they behave in a case where the internal damping is smaller than the optimal value ($\sigma = 0.05$, $\epsilon = 0.1$, $x_c = 0.72$m in this second case). Indeed, it has appeared interesting to show this case since the optimal

19

damping value is very large and probably difficult to implement in a practical situation. The amplitude of the external force A is increased from 0.01 to 100N.
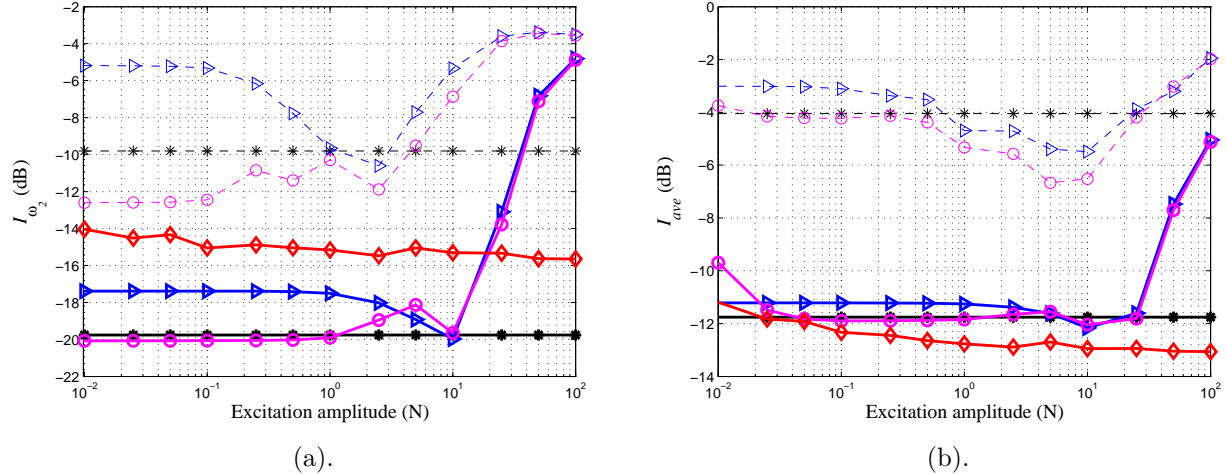

(a).   (b).

Fig. 11. Robustness of indicators in each cases to forcing amplitude, (a): value of I_{ω_2}, (b): value of I_{ave}. Solid line: the optimal parameters, dashed line: comparison in the weak damping case. dashed black: TMD with $k_l = 500$N/m and weak damping $\sigma = 0.05$N$\cdot$s/m; solid black: TMD with optimized parameters $\sigma = 2$N$\cdot$s/m and $k_l = 500$N/m; dashed blue: NES with $k_n = 2 \times 10^9$N/m^3 and weak damping $\sigma = 0.05$N$\cdot$s/m; solid blue: NES with optimized parameters $\sigma = 2$N$\cdot$s/m and $k_n = 2 \times 10^9$N/m^3; dashed magenta: BNES with $k_n = 2 \times 10^9$N/m^3, $k_l = -300$N/m, and weak damping $\sigma = 0.05$N$\cdot$s/m; solid magenta: BNES with optimized parameters $\sigma = 2$N$\cdot$s/m, $k_l = -300$N/m, and $k_n = 2 \times 10^9$N/m^3; red: VI-ABH, optimized parameters with $k_n = 10^9$N/m$^{1.5}$ and x_c=0.2m

The three absorbers show major differences on the effect of the forcing amplitudes. First, as it can be expected, the TMD is always independent to the amplitude, the indicator at all the excitation level is the same and the performance is linear. Second, the NES is highly dependent on the amplitude. Fig. 11(a) shows the energy barrier: below 0.1N, the performance of I_{ω_2} is weak and start to increase to meet an optimal performance around 2.5N, and then again deteriorates at very large amplitudes. The energy barrier for the BNES is less clear but as in the case of the NES, the performance decreases at very large amplitudes. This is also evidenced on the behaviour of I_{ave} reported in Fig. 11(b). One can note however that adding a negative stiffness in the NES to realize a BNES leads to an improvement of the performance at low amplitudes. All these results show that all the proposed solutions are able to achieve good broadband vibration mitigation, with slight differences between the retained solutions.

4. Conclusion

In this contribution, the effect of adding a single vibration absorber to an ABH beam, in order to achieve a broadband vibration mitigation, is discussed. Three different vibration absorbers have been contrasted : a TMD, and two nonlinear absorbers, a NES and a BNES. The proposed solutions have also been compared to a Vibro-Impact ABH (VI-ABH), which is another strategy proposed to enhance the low-frequency efficiency of an ABH by adding contact points to generate shocks. The numerical results clearly shows that, when appropriately designed, all the methods could be effective to reduce the low frequency resonance peaks in the ABH beam, with a reduction at more than 10dB.

A parametric study has been conducted in order to optimize the tunings of the different absorbers and to understand the operating modes of the devices. In particular, numerous results from the literature has been retrieved and highlighted on an ABH beam. The performance of the TMD has been shown to be independent of the excitation level, in line with its linear behaviour. On the other hand, NES and BNES outperform the TMD for small values of internal damping in the vibration absorber, but for large values of this damping,energy transfer is reduced and the nonlienar absorbers behave linearly. The dependence on the vibration amplitude has also been studied, showing that a NES can generally be effective with moderate excitation level, while using a BNES could improve its performance for small amplitude of vibrations. On the other hand, the performances of these two solutions deteriorates for very high vibration amplitudes.

The VI-ABH has been found to perform robustly and effectively. The contact stiffness plays an important role, while for the location of a single contact point, the tuning rule is more complicated than that found for nonlinear dampers, but one can still see the relationship with mode shapes.

All these findings show that these solutions can be used in order to achieve an important gain in the low-frequency efficiency of an ABH beam.

Appendix A. Complex bending stiffness and the eigenvalue problem

For a viscoelastic layer added in $[x_{abh}, L]$ with thickness h_l, the complex bending stiffness $D^*(x)$ reads

$$D^*(x) = \begin{cases} E_b I_b(x) \left(1 + j\eta_b\right), & \forall x \in [0, x_{abh}], \\ E_b I_b(x) \left[(1 + j\eta_b) + \dfrac{E_l}{E_b} \left(\dfrac{h_l}{h_b(x)}\right)^3 (1 + j\eta_l) + \right. \\ \left. \dfrac{3 \left(1 + \frac{h_l}{h_b(x)}\right)^2 \frac{E_l h_l}{E_b h_b(x)} \left(1 - \eta_b \eta_l + j\left(\eta_b + \eta_l\right)\right)}{1 + \frac{E_l h_l}{E_b h_b(x)} (1 + j\eta_l)} \right], & \forall x \in [x_{abh}, L], \end{cases} \tag{A.1}$$

where j is the imaginary unit, E_b, I_b, and η_b are respectively the Young modulus, the moment of inertia and the loss factor of the beam alone, while E_l and η_l corresponds to the Young

modulus and the loss factor of the viscoelastic layer. With this expression, the damping term is thus considered to be linear, based on the assumption that the vibration amplitude is small as compared to the beam thickness in the uniform area. In the case where geometric nonlinearity may be activated, a nonlinear damping could occur and hence brings about small differences; with increasing damping levels when increasing the vibration amplitudes, see *e.g.* [57]. In this paper, our main focus is to investigate independently the effects brought by different types of nonlinear absorbers, thus the ABH beam and its damping are assumed to be linear.

The eigenvalue problem mentioned in section 2.3 is formulated by solving Eq. (2a) with $f = p = 0$. A finite difference method with a non-uniform grid spacing is used, following [5, 50, 61]. Practically, a coordinate change is introduced that maps the physical coordinate $x \in [0, L]$ onto a uniform mesh grid $\lambda \in [0, 1]$. The map between λ and x is selected according to the variations of the flexural wavelength and reads :

$$\lambda(x) = \frac{1}{\bar{X}} \int_0^x \frac{1}{\sqrt{h(\theta)}} \mathrm{d}\theta \,, \qquad \text{with} \qquad \bar{X} = \int_0^L \frac{1}{\sqrt{h(\theta)}} \mathrm{d}\theta \,. \tag{A.2}$$

The uniform grid spacing λ_l is then simply introduced as $\lambda_l = l\Delta_\lambda$, for $l = 1, ..., N_\lambda$, with $\Delta_\lambda = 1/N_\lambda$ the spatial step. All the functional fields appearing in the linearized Eq. (2) are computed on these grid points, with for example $D_l = D(\lambda_l)$, $\rho_l = \rho(\lambda_l)$, ... The eigenvalue problems to be solved can then be expressed in λ and reads:

$$-\rho_l A_l \omega^2 \phi_l + \frac{h_l^{-1/2}}{\bar{X}^4} \delta_{\lambda+} \left(\left(\mu_{\lambda-} h_l^{-1/2} \right) \delta_{\lambda-} \left(D_l h_l^{-1/2} \delta_{\lambda+} \left(\left(\mu_{\lambda-} h_l^{-1/2} \right) \delta_{\lambda-} \phi_l \right) \right) \right) = 0. \tag{A.3}$$

where the spatial difference operators $\delta_{\lambda+}$, $\delta_{\lambda-}$ and the averaging operator $\mu_{\lambda-}$ are defined as

$$\delta_{\lambda+} u = \frac{u_{l+1} - u_l}{\Delta_\lambda}, \ \delta_{\lambda-} u = \frac{u_l - u_{l-1}}{\Delta_\lambda}, \ \mu_{\lambda-} u = \frac{u_l + u_{l-1}}{2}. \tag{A.4}$$

The discrete boundary conditions in Eq. (3) can be expressed as

$$u_0 = u_1 = 0, \tag{A.5}$$

for the clamped boundary condition in $x = 0$, and

$$\delta_{\lambda+} \left(\left(\mu_{\lambda-} \phi^{-1/2} \right) \delta_{\lambda-} u_N \right) = \delta_{\lambda+} \left(\left(\mu_{\lambda-} \phi^{-1/2} \right) \delta_{\lambda-} u_{N-1} \right) = 0, \tag{A.6}$$

for the free boundary condition at $x = L$, respectively.

To solve the eigenvalue problem, Eq. (A.3) is computed separately two times. For the first computation, the real part of the bending stiffness $D(x) = \mathrm{Re}(D^*(x))$ is used, giving the undamped eigenmode shape $\varphi_k(x)$ and the radian eigenfrequency ω_k for the ABH beam, with $k = 1, ..., N_m$. Taking losses into account, a second computation is then realized, but considering the complex bending stiffness D^* introduced in Eq. (A.1). As a result, complex eigenfrequencies $\omega_k^\star$ are retrieved, whose relationship to those obtained real ω_k writes

$$j\omega_k^\star = \omega_k \left(-\xi_k \pm j\sqrt{1 - \xi_k^2} \right), \tag{A.7}$$

22

with ξ_k the unknown modal damping ratio. From Eq. (A.7), together with the computed ω_k and $\omega_k^\star$, the modal damping ratios ξ_k in Eqs. (5) can thus be identified.

Appendix B. Numerical details on the time integration method

Let $t_n = n\Delta t$, with n the step index and Δt the time step. A special feature of the numerical integrator developed in [58] is to use the modal approach for the linear part, whereas the coupling force is computed in the physical space. To that purpose, the relationship between modal space and physical space needs to be explicated, which is realized by introducing $\mathbf{S}_F = [\phi_1(x_F),\ \phi_2(x_F),\ \cdots,\ \phi_{N_m}(x_F)]$ as the modal vector containing the first N_m beam modes at x_F, and $\mathbf{S}_c = [\phi_1(x_c),\ \phi_2(x_c),\ \cdots,\ \phi_{N_m}(x_c)]$ the modal vector at x_c. The relationship with the modal expansion (4) allows one to write $u(x_c, n\Delta t) = \mathbf{S}_c \mathbf{q^n}$, and $u(x_F, n\Delta t) = \mathbf{S}_F \mathbf{q^n}$, where $\mathbf{q^n} = [q_1(n\Delta t), q_2(n\Delta t),\ \cdots,\ q_{N_m}(n\Delta t)]^T$. For each time step n, the equation of motion for the system in Eqs. (5) can be rewritten as:

$$\mathbf{q}^{n+1} = \mathbf{C}\mathbf{q}^n - \tilde{\mathbf{C}}\mathbf{q}^{n-1} + \Delta t^2 \left(\mathbf{S}_F^T p^n - \mathbf{S}_c^T f^n \right), \tag{B.1a}$$

$$m\delta_t v^n = f^n, \tag{B.1b}$$

$$f^n = k_l w^n + k_n (w^n)^2 \mu_t w^n + 2\sigma \delta_t w^n, \tag{B.1c}$$

$$w^n = \mathbf{S}_c \mathbf{q^n} - v^n. \tag{B.1d}$$

where p^n and f^n are respectively the external and restoring forces computed at time n. $\mathbf{C}$ and $\tilde{\mathbf{C}}$ are two diagonal matrices, whose entries are

$$C_{kk} = e^{-\omega_k \xi_k \Delta t} \left(e^{\omega_k \sqrt{\xi_k^2 - 1}\Delta t} + e^{-\omega_k \sqrt{\xi_k^2 - 1}\Delta t} \right), \quad \tilde{C}_{kk} = e^{-2\omega_k \xi_k \Delta t}. \tag{B.2}$$

δ_t is a centred time difference reading $\delta_t w^n = (w^{n+1} - w^{n-1})/2\Delta t$, and μ_t is an averaging operator: $\mu_t w^n = (w^{n+1} + w^{n-1})/2$. Note that the particular choice of the matrices and operators are related to an exact energy conserving scheme for the free flight phases of the vibration [58, 61].

Denoting then $\mathbf{Q} = \left[\mathbf{q}^T, v\right]^T$, $\mathbf{S}_{qF} = [\mathbf{S}_F, 0]$, and $\mathbf{S}_{qc} = [\mathbf{S}_c, -1]$, the four equations the four equations in Eq.(B.1) can finally be combined into a simple matrix form as

$$\mathbf{C}_1 \mathbf{Q}^{n+1} = \mathbf{C}_2 \mathbf{Q}^n - \mathbf{C}_3 \mathbf{Q}^{n-1} + \Delta t^2 \mathbf{S}_{qF}^T p^n - \Delta t^2 \mathbf{S}_{qc}^T f^n \tag{B.3}$$

with

$$\mathbf{C}_1 = \begin{bmatrix} \mathbf{I}_{N_m} & \\ & m \end{bmatrix}, \mathbf{C}_2 = \begin{bmatrix} \mathbf{C} & \\ & 2m \end{bmatrix}, \mathbf{C}_3 = \begin{bmatrix} \tilde{\mathbf{C}} & \\ & m \end{bmatrix} \tag{B.4}$$

On the other hand, implying the relationship $w = \mathbf{S}_{qc}\mathbf{Q}$, the restoring force can be calculated as

$$f^n = -k_l \mathbf{S}_{qc}\mathbf{Q}^n + \left[\frac{k_n (\mathbf{S}_{qc}\mathbf{Q}^n)^2}{2} + \frac{\sigma}{\Delta t} \right] \mathbf{S}_{qc}\mathbf{Q}^{n+1} + \left[\frac{k_n (\mathbf{S}_{qc}\mathbf{Q}^n)^2}{2} - \frac{\sigma}{\Delta t} \right] \mathbf{S}_{qc}\mathbf{Q}^{n-1} \tag{B.5}$$

Finally, eliminating the force term f^n yields

$$\mathbf{C}_{n+1}\mathbf{Q}^{n+1} = \mathbf{C}_n\mathbf{Q}^n - \mathbf{C}_{n-1}\mathbf{Q}^{n-1} + \mathbf{C}_F p^n \tag{B.6}$$

where

$$\begin{aligned}
\mathbf{C}_{n+1} &= \mathbf{C}_1 + \frac{\Delta t^2 k_n (\mathbf{S}_{qc}\mathbf{Q}^n)^2}{2}\mathbf{S}_{qc}^T\mathbf{S}_{qc} + \sigma\Delta t\mathbf{S}_{qc}^T\mathbf{S}_{qc} \\
\mathbf{C}_n &= \mathbf{C}_2 - \Delta t^2 k_l\mathbf{S}_{qc}^T\mathbf{S}_{qc} \\
\mathbf{C}_{n-1} &= \mathbf{C}_3 + \frac{\Delta t^2 k_n (\mathbf{S}_{qc}\mathbf{Q}^n)^2}{2}\mathbf{S}_{qc}^T\mathbf{S}_{qc} - \sigma\Delta t\mathbf{S}_{qc}^T\mathbf{S}_{qc} \\
\mathbf{C}_F &= \Delta t^2\mathbf{S}_{qF}^T
\end{aligned} \tag{B.7}$$

Eq. (B.6) is used to compute the update of the system at time step n to $n+1$.

Appendix C. Equations for the VI-ABH

According to [22], the governing equation for a VI-ABH depicted in Fig. 1(b) can be expressed as

$$\rho(x)A(x)\frac{\partial^2 u}{\partial t^2} + \frac{\partial^2}{\partial x^2}\left(D(x)\frac{\partial^2 u}{\partial x^2}\right) = p\delta(x - x_F) + g\delta(x - x_c). \tag{C.1}$$

The equation is numerically treated in the same manner, the only difference is to replace the restoring force by the contact force, and the update equation to solve now reads

$$\mathbf{q}^{n+1} = \mathbf{C}\mathbf{q}^n - \tilde{\mathbf{C}}\mathbf{q}^{n-1} + \Delta t^2\left(\mathbf{S}_F^T p^n + \mathbf{S}_c^T g^n\right), \tag{C.2}$$

while the contact force is computed via

$$g^n = \frac{\psi(\eta^{n+1}) - \psi(\eta^{n-1})}{\eta^{n+1} - \eta^{n-1}}, \tag{C.3}$$

with $\eta = h_c - u(x_c, t)$ the interpenetration displacement of the beam into the contact barrier, and where the potential function describing the contact force is defined by $\psi(x,t) = \frac{k_c}{\alpha+1}[\eta]_+^{\alpha+1}$, with $[\eta]_+ = \frac{1}{2}(\eta + |\eta|)$ (see [22, 58, 62]). Note finally that due to the the nonlinear character of the contact force, the scheme is implicit and a Newton-Raphson iteration is hence applied for the update of Eq. (C.2).

[1] V.V. Krylov and F.J.B.S. Tilman. Acoustic black holes for flexural waves as effective vibration dampers. *Journal of Sound and Vibration*, 274(3-5):605–619, 2004.

[2] A. Pelat, F. Gautier, S.C. Conlon, and F. Semperlotti. The acoustic black hole: A review of theory and applications. *Journal of Sound and Vibration*, page 115316, 2020.

[3] V.B. Georgiev, J. Cuenca, F. Gautier, L. Simon, and V.V. Krylov. Damping of structural vibrations in beams and elliptical plates using the acoustic black hole effect. *Journal of sound and vibration*, 330(11):2497–2508, 2011.

[4] L. Tang, L. Cheng, H. Ji, and J. Qiu. Characterization of acoustic black hole effect using a one-dimensional fully-coupled and wavelet-decomposed semi-analytical model. *Journal of Sound and Vibration*, 374:172 – 184, 2016.

[5] V. Denis, A. Pelat, F. Gautier, and B. Elie. Modal overlap factor of a beam with an acoustic black hole termination. *Journal of Sound and Vibration*, 333(12):2475–2488, 2014.

[6] D.J. O'Boy, V.V. Krylov, and V. Kralovic. Damping of flexural vibrations in rectangular plates using the acoustic black hole effect. *Journal of Sound and Vibration*, 329(22):4672–4688, 2010.

[7] M.R. Shepherd, C.A. McCormick, S.C. Conlon, and P.A. Feurtado. Modeling and optimization of acoustic black hole vibration absorbers. *The Journal of the Acoustical Society of America*, 141(5):4034–4034, 2017.

[8] L. Tang and L. Cheng. Enhanced acoustic black hole effect in beams with a modified thickness profile and extended platform. *Journal of Sound and Vibration*, 391:116 – 126, 2017.

[9] J. Leng, V. Romero-García, A. Pelat, R. Picó, J-P. Groby, and F. Gautier. Interpretation of the acoustic black hole effect based on the concept of critical coupling. *Journal of Sound and Vibration*, page 115199, 2020.

[10] V.V. Krylov and R.E.T.B. Winward. Experimental investigation of the acoustic black hole effect for flexural waves in tapered plates. *Journal of Sound and Vibration*, 300(1-2):43–49, 2007.

[11] V. Denis, F. Gautier, A. Pelat, and J. Poittevin. Measurement and modelling of the reflection coefficient of an acoustic black hole termination. *Journal of Sound and Vibration*, 349:67–79, 2015.

[12] E.P. Bowyer, D.J. O'Boy, V.V. Krylov, and F. Gautier. Experimental investigation of damping flexural vibrations in plates containing tapered indentations of power-law profile. *Applied Acoustics*, 74(4):553–560, 2013.

[13] P.A. Feurtado and S.C. Conlon. An experimental investigation of acoustic black hole dynamics at low, mid, and high frequencies. *Journal of Vibration and Acoustics*, 138(6):061002, 2016.

[14] J.Y. Lee and W. Jeon. Exact solution of euler-bernoulli equation for acoustic black holes via generalized hypergeometric differential equation. *Journal of Sound and Vibration*, 452:191–204, 2019.

[15] K. Hook, J. Cheer, and S. Daley. A parametric study of an acoustic black hole on a beam. *The Journal of the Acoustical Society of America*, 145(6):3488–3498, 2019.

[16] L. Lagny, M. Secail-Geraud, J. Le Meur, S. Montrésor, K. Heggarty, C. Pezerat, and P. Picart. Visualization of travelling waves propagating in a plate equipped with 2d abh using wide-field holographic vibrometry. *Journal of Sound and Vibration*, 461:114925, 2019.

[17] C.A. McCormick and M.R. Shepherd. Design optimization and performance comparison of three styles of one-dimensional acoustic black hole vibration absorbers. *Journal of Sound and Vibration*, 470:115164, 2020.

[18] C. Zhao and M.G. Prasad. Acoustic black holes in structural design for vibration and noise control. In *Acoustics*, volume 1, pages 220–251. Multidisciplinary Digital Publishing Institute, 2019.

[19] J. Deng, L. Zheng, P. Zeng, Y. Zuo, and O. Guasch. Passive constrained viscoelastic layers to improve the efficiency of truncated acoustic black holes in beams. *Mechanical Systems and Signal Processing*, 118:461 – 476, 2019.

[20] L. Tang and L. Cheng. Broadband locally resonant band gaps in periodic beam structures with embedded acoustic black holes. *Journal of Applied Physics*, 2017.

[21] L. Zhao, S.C. Conlon, and F. Semperlotti. Broadband energy harvesting using acoustic black hole structural tailoring. *Smart Materials and Structures*, 23(6):065021, 2014.

[22] H. Li, C. Touzé, A. Pelat, F. Gautier, and X. Kong. A vibro-impact acoustic black hole for passive damping of flexural beam vibrations. *Journal of Sound and Vibration*, 450:28–46, 2019.

[23] S.C. Conlon, J.B. Fahnline, and F. Semperlotti. Numerical analysis of the vibroacoustic properties of plates with embedded grids of acoustic black holes. *The Journal of the Acoustical Society of America*, 137(1):447–457, 2015.

[24] O. Aklouche, A. Pelat, S. Maugeais, and F. Gautier. Scattering of flexural waves by a pit of quadratic profile inserted in an infinite thin plate. *Journal of Sound and Vibration*, 375:38–52, 2016.

[25] S.C. Conlon and P.A. Feurtado. Progressive phase trends in plates with embedded acoustic black holes. *The Journal of the Acoustical Society of America*, 143(2):921–930, 2018.

[26] J.P. Den Hartog. *Mechanical Vibrations*. McGraw-Hill, New-York, 1934.

[27] H.C. Tsai and G.C. Lin. Optimum tuned mass dampers for minimizing steady-state response of support excited and damped system. *Earthquake Engineering and Structural Dynamics*, 11:846–862, 1993.

[28] C.L. Lee, Y.T. Chen, L.L. Chung, and Y.P. Wang. Optimal design theories and applications of tuned mass dampers. *Engineering structures*, 28(1):43–53, 2006.

[29] S. Krenk and J. Hogsberg. Tuned mass absorber on a flexible structure. *Journal of Sound and Vibration*, 333:1577–1595, 2014.

[30] A.F. Vakakis and O.V. Gendelman. Energy pumping in nonlinear mechanical oscillators: part iiresonance capture. *Journal of Applied Mechanics*, 68(1):42–48, 2001.

[31] A.F. Vakakis, L.I. Manevitch, O.V. Gendelman, and L. Bergman. Dynamics of linear discrete systems connected to local, essentially non-linear attachments. *Journal of Sound and Vibration*, 264(3):559–577, 2003.

[32] O.V. Gendelman, Y. Starosvetsky, and M. Feldman. Attractors of harmonically forced linear oscillator with attached nonlinear energy sink i: description of response regimes. *Nonlinear Dynamics*, 51(1-2):31–46, 2008.

[33] M. Parseh, M. Dardel, and M.H. Ghasemi. Performance comparison of nonlinear energy sink and linear tuned mass damper in steady-state dynamics of a linear beam. *Nonlinear Dynamics*, 81(4):1981–2002, 2015.

[34] Y. Starosvetsky and O.V. Gendelman. Attractors of harmonically forced linear oscillator with attached nonlinear energy sink. ii: Optimization of a nonlinear vibration absorber. *Nonlinear Dynamics*, 51(1-2):47, 2008.

[35] M.A. Al-Shudeifat. Nonlinear energy sinks with nontraditional kinds of nonlinear restoring forces. *Journal of Vibration and Acoustics*, 139(2), 2017.

[36] Y. Starosvetsky and O.V. Gendelman. Vibration absorption in systems with a nonlinear energy sink: nonlinear damping. *Journal of Sound and Vibration*, 324(3-5):916–939, 2009.

[37] X. Kong, H. Li, and C. Wu. Dynamics of 1-dof and 2-dof energy sink with geometrically nonlinear damping: application to vibration suppression. *Nonlinear Dynamics*, 91(1):733–754, 2018.

[38] O.V. Gendelman. Analytic treatment of a system with a vibro-impact nonlinear energy sink. *Journal of Sound and Vibration*, 331(21):4599–4608, 2012.

[39] E. Gourc, G. Michon, S. Seguy, and A. Berlioz. Targeted energy transfer under harmonic forcing with a vibro-impact nonlinear energy sink: analytical and experimental developments. *Journal of Vibration and Acoustics*, 137(3):031008, 2015.

[40] D. M. McFarland, L. A. Bergman, and A. F. Vakakis. Experimental study of non–linear energy pumping occurring at a single fast frequency. *Int. Journal of Non–linear Mechanics*, 40:891 – 899, 2005.

[41] M. A. Al-Shudeifat. Asymmetric magnet–based nonlinear energy sink. *Journal of Computational and Nonlinear Dynamics*, 10(1):014502, 2014.

[42] S. Benacchio, A. Malher, J. Boisson, and C. Touzé. Design of a Magnetic Vibration Absorber with tunable stiffnesses. *Nonlinear Dynamics*, 85:893 – 911, 2016.

[43] P. Soltani and G. Kerschen. The nonlinear piezoelectric tuned vibration absorber. *Smart Materials and Structures*, 24(7):075015, 2015.

[44] G. Pennisi, C. Stephan, E. Gourc, and G. Michon. Experimental investigation and analytical description of a vibro–impact NES coupled to a single–degree–of–freedom linear oscillator harmonically forced. *Nonlinear Dynamics*, 88(3):1769 – 1784, 2017.

[45] G. Pennisi, B. P. Mann, N. Naclerio, C. Stephan, and G. Michon. Magnetic–strung NES with energy harvesting: theoretical and experimental study of a new concept of nonlinear vibration absorber. *Journal of Sound and Vibration*, submitted.

[46] S. Lo Feudo, C. Touzé, J. Boisson, and G. Cumunel. Nonlinear magnetic vibration absorber for passive control of a multistorey structure. *Journal of Sound and Vibration*, 438:33 – 53, 2019.

[47] F. Romeo, G. Sigalov, L.A. Bergman, and A.F. Vakakis. Dynamics of a linear oscillator coupled to a bistable light attachment: numerical study. *Journal of Computational and Nonlinear Dynamics*, 10(1), 2015.

[48] L.I. Manevitch, G. Sigalov, F. Romeo, L.A. Bergman, and A.F. Vakakis. Dynamics of a linear oscillator coupled to a bistable light attachment: analytical study. *Journal of Applied Mechanics*, 81(4), 2014.

[49] G. Habib and F. Romeo. The tuned bistable nonlinear energy sink. *Nonlinear Dynamics*, 89(1):179–196, 2017.

[50] V. Denis, A. Pelat, C. Touzé, and F. Gautier. Improvement of the acoustic black hole effect by using energy transfer due to geometric nonlinearity. *International Journal of Non-Linear Mechanics*, 94:134–145, 2017.

[51] R.P. Goel. Transverse vibrations of tapered beams. *Journal of Sound and Vibration*, 47(1):1 – 7, 1976.

[52] J.R. Banerjee and F.W. Williams. Exact Bernoulli-Euler dynamic stiffness matrix for a range of tapered beams. *International Journal for Numerical Methods in Engineering*, 21(12):2289–2302, 1985.

[53] Y.S. Lee, A.F. Vakakis, L.A. Bergman, D.M. McFarland, G. Kerschen, F. Nucera, S. Tsakirtzis, and P.N. Panagopoulos. Passive non-linear targeted energy transfer and its applications to vibration absorption: a review. *Proceedings of the Institution of Mechanical Engineers, Part K: Journal of Multi-body Dynamics*, 222(2):77–134, 2008.

[54] J. Zang and L. Chen. Complex dynamics of a harmonically excited structure coupled with a nonlinear energy sink. *Acta Mechanica Sinica*, 33(4):801–822, 2017.

[55] D. Qiu, T. Li, S. Seguy, and M. Paredes. Efficient targeted energy transfer of bistable nonlinear energy sink: application to optimal design. *Nonlinear Dynamics*, 92(2):443–461, 2018.

[56] D. Ross, E.E. Ungar, and E.M. Kerwin. Damping of plate flexural vibrations by means of viscoelastic laminae. *Structural damping*, pages 49–97, 1959.

[57] Marco Amabili. Derivation of nonlinear damping from viscoelasticity in case of nonlinear vibrations. *Nonlinear Dynamics*, 97(3):1785–1797, 2019.

[58] C. Issanchou, S. Bilbao, J.L. Le Carrou, C. Touzé, and O. Doaré. A modal-based approach to the nonlinear vibration of strings against a unilateral obstacle: Simulations and experiments in the pointwise case. *Journal of Sound and Vibration*, 393:229–251, 2017.

[59] T. Asami, O. Nishihara, and A.M. Baz. Analytical solutions to H∞ and H$_2$ optimization of dynamic vibration absorbers attached to damped linear systems. *J. Vib. Acoust*, 124(2):284 – 295, 2002.

[60] F.S. Samani and F. Pellicano. Vibration reduction of beams under successive traveling loads by means of linear and nonlinear dynamic absorbers. *Journal of Sound and Vibration*, 331(10):2272–2290, 2012.

[61] S. Bilbao. *Numerical sound synthesis: finite difference schemes and simulation in musical acoustics*. John Wiley & Sons, Edinburgh, 2009.

[62] S. Bilbao, A. Torin, and V. Chatziioannou. Numerical modeling of collisions in musical instruments. *Acta Acustica united with Acustica*, 101(1):155–173, 2015.